Scalar-Induced Gravitational Waves and Primordial Black Holes from a Localized Bump or Dip Feature in a Single-Field Inflationary Potential

Xiang Zhang[1] and Zhao-Huan Yu[1,*]

[1] *School of Physics, Sun Yat-Sen University, Guangzhou 510275, China*

We study the production of scalar-induced gravitational waves and primordial black holes in a single-field inflation model with a localized bump or dip feature in the potential. Introducing such a localized feature temporarily decelerates the slow-roll inflaton, amplifying the primordial curvature power spectrum into a sharp peak. Consequently, this enhancement sources a significant stochastic background of gravitational waves and leads to abundant formation of primordial black holes. Through eight benchmark cases, we show that the predicted abundances of primordial black holes can remain compatible with current observational limits, while the corresponding gravitational wave spectra peaking across a wide range of frequencies are accessible to future gravitational wave experiments in multiple observational bands.

CONTENTS

* Corresponding author. yuzhaoh5@mail.sysu.edu.cn

I. INTRODUCTION

Inflation resolves a lot of problems that plague the standard cosmological model, such as the flatness, horizon, and monopole problems [1–4]. During inflation, primordial curvature perturbations are stretched outside the Hubble horizon and their amplitudes freeze at certain values. Inflation predicts a nearly scale-invariant spectrum for these perturbations, which is highly consistent with observations of the cosmic microwave background (CMB) [5]. Specifically, CMB observations suggest that the amplitude of the power spectrum of curvature perturbations, $\mathcal{P}_\zeta$, is about 2.1×10^{-9} at the pivot scale $k_* = 0.05\ \mathrm{Mpc}^{-1}$ [5].

After inflation, these super-horizon perturbations reenter the Hubble radius during the radiation- or matter-dominated era, seeding the formation of large-scale cosmic structures and also potentially resulting in the generation of primordial black holes (PBHs) [6–10]. Specifically, primordial overdensities caused by horizon reentry of modes with significantly amplified power spectrum $\mathcal{P}_\zeta$ would collapse to form PBHs. In the standard slow-roll inflation, however, the possibility of PBH production is slim, as the predicted amplitude of the power spectrum ($\mathcal{P}_\zeta \sim 10^{-9}$) is too small. To generate an abundant population of PBHs, $\mathcal{P}_\zeta$ is required to reach $\mathcal{O}(10^{-2})$. Since CMB observations have only placed stringent constraints on $\mathcal{P}_\zeta$ at large scales, the production of abundant PBHs can be achieved by enhancing the power spectrum amplitude by seven orders of magnitude at small scales.

When such amplified curvature perturbations reenter the Hubble horizon during the radiation-dominated era, they not only generate PBHs but also source considerable scalar-induced gravitational waves (SIGWs) as a second-order effect, contributing to the stochastic gravitational wave background (SGWB) [11–35]. Excitingly, four major pulsar timing array (PTA) collaborations, NANOGrav [36, 37], PPTA [38, 39], EPTA [40, 41], and CPTA [42], have announced strong evidence of an SGWB signal in 2023. SIGWs are a promising candidate to explain this signal, providing a compelling and timely motivation to study PBHs and gravitational waves (GWs) originated from primordial curvature perturbations.

In the context of single-field inflation models, achieving such a small-scale enhancement typically requires particular features in the inflaton potential. For instance, a near-inflection point or a saddle-type region can slow the motion of the inflaton field, leading to a spike in the curvature power spectrum [43–49]. Alternatively, the slow-roll evolution of the inflaton can be briefly disrupted by a small, localized feature in its potential, leading to an enhancement of curvature perturbations [50]. In this work, we study two kinds of such features: a localized bump and a localized dip.

Because of their interplay with Hubble friction, both features can cause a temporary deceleration of the inflaton, leading to a sharp peak in the primordial curvature power spectrum. We apply this simple prescription to the Kachru-Kallosh-Linde-Trivedi (KKLT) inflation model based on the string theory [51, 52] by adding a term $V_{\rm base}(\phi)\varepsilon(\phi)$ with $\varepsilon(\phi) \ll 1$, localized at $\phi = \phi_{\rm d}$, to the base inflationary potential $V_{\rm base}(\phi)$. This mechanism produces a sharp, localized enhancement of primordial perturbations around $\phi_{\rm d}$, which could lead to a significant abundance of PBHs and essential emissions of SIGWs. In the work, we investigate the predicted PBH abundance and the resulting SIGW spectrum, and explore the implications for related phenomenology.

The paper is organized as follows. In Sec. II we summarize the essentials of single-field inflation.

Sec. III reviews the production of SIGWs, while Sec. IV outlines the basics of PBH formation. Our numerical framework and main results are presented in Sec. V. Finally, we give our conclusions in Sec. VI.

II. INFLATION AND PRIMORDIAL CURVATURE PERTURBATIONS

The simplest models of inflation involve a single scalar field ϕ, i.e., the inflaton field. The dynamics of ϕ minimally coupled to gravity is governed by the action

$$S=\int \mathrm{d}^4x\sqrt{-g}\left[\frac{1}{2}m_{\rm Pl}^2R+\frac{1}{2}g^{\mu\nu}\partial_\mu\phi\,\partial_\nu\phi-V(\phi)\right], \tag{1}$$

where $m_{\rm Pl}$ is the reduced Planck mass, R is the Ricci scalar, and the potential $V(\phi)$ describes the self-interactions of the inflaton field.

For the spatially flat Friedmann-Robertson-Walker metric, the line element is given by $\mathrm{d}s^2=-\mathrm{d}t^2+a^2(t)\mathrm{d}\boldsymbol{x}^2$, where $a(t)$ is the scale factor. The background evolution of the inflaton field and the scale factor is governed by the following set of cosmological equations

$$\begin{cases} 3m_{\rm Pl}^2H^2=\rho_\phi=\dfrac{1}{2}\dot{\phi}^2+V(\phi), \\ \dot{H}=\dfrac{\ddot{a}}{a}-H^2=-\dfrac{1}{2m_{\rm Pl}^2}\dot{\phi}^2, \\ \ddot{\phi}+3H\dot{\phi}+V'(\phi)=0, \end{cases} \tag{2}$$

where an overdot denotes the derivative with respect to the cosmic time t, $H=\dot{a}/a$ is the Hubble parameter, and $V'(\phi)=\mathrm{d}V/\mathrm{d}\phi$.

The extent of inflation is indicated by the e-folding number N, defined as

$$N(t)=\int_{t_{\rm ini}}^{t}H(\tilde{t})\,\mathrm{d}\tilde{t}=\int_{\phi(t_{\rm ini})}^{\phi(t)}\frac{H}{\mathrm{d}\tilde{\phi}/\mathrm{d}t}\,\mathrm{d}\tilde{\phi}, \tag{3}$$

where $t_{\rm ini}$ denotes the initial time of inflation. To solve the main problems of the standard hot Big Bang model, a period of quasi-de-Sitter expansion lasting for at least 60–70 e-folds is generally required. This can be achieved by a slowly rolling inflaton field. We adopt $N_*=58$ as the e-folding number remaining from the moment the CMB pivot scale $k_*=0.05\ \mathrm{Mpc}^{-1}$ left the Hubble radius until the end of inflation. The slow-roll phase of inflation is usually characterized by two Hubble slow-roll parameters [53]

$$\epsilon_H\equiv-\frac{\dot{H}}{H^2}=\frac{1}{2m_{\rm Pl}^2}\left(\frac{\mathrm{d}\phi}{\mathrm{d}N}\right)^2, \tag{4}$$

$$\eta_H\equiv-\frac{\ddot{\phi}}{H\dot{\phi}}=\epsilon_H-\frac{1}{2\epsilon_H}\frac{\mathrm{d}\epsilon_H}{\mathrm{d}N}. \tag{5}$$

Using the horizon-crossing condition $k=aH$, we can establish the relationship between the comoving wavenumber k and the field value ϕ through

$$k(\phi)=H(\phi)a(\phi)=H(\phi)a(t_{\rm ini})\exp\left(\int_{\phi(t_{\rm ini})}^{\phi}\frac{H}{\mathrm{d}\tilde{\phi}/\mathrm{d}t}\,\mathrm{d}\tilde{\phi}\right). \tag{6}$$

For a homogeneous and isotropic universe, the two-point correlation function of primordial curvature perturbations reads

$$\langle\zeta(\boldsymbol{k})\zeta(\tilde{\boldsymbol{k}})\rangle \equiv (2\pi)^3\delta(\boldsymbol{k}+\tilde{\boldsymbol{k}})\,P_\zeta(k) \equiv (2\pi)^3\delta(\boldsymbol{k}+\tilde{\boldsymbol{k}})\,\frac{2\pi^2}{k^3}\,\mathcal{P}_\zeta(k), \tag{7}$$

where $P_\zeta(k)$ is the power spectrum of curvature perturbations and $\mathcal{P}_\zeta(k)$ is its dimensionless version. Under the slow-roll approximation, where the conditions $\epsilon_H \ll 1$ and $\eta_H \ll 1$ are satisfied, $\mathcal{P}_\zeta(k)$ is roughly given by [53]

$$\mathcal{P}_\zeta(k) = \frac{1}{8\pi^2}\left(\frac{H_k}{m_{\rm Pl}}\right)^2\frac{1}{\epsilon_{H,k}}, \tag{8}$$

where the subscript k indicates that H and ϵ_H are evaluated at the Hubble crossing $k = aH$.

The dimensionless power spectrum $\mathcal{P}_\zeta$ can be determined more accurately by making use of the Mukhanov-Sasaki equation [54, 55]

$$v_k'' + \left(k^2 - \frac{z''}{z}\right)v_k = 0, \tag{9}$$

where $v \equiv z\zeta$ is the Mukhanov-Sasaki variable with $z = a\dot{\phi}/H$. A prime ($'$) denotes differentiation with respect to the conformal time η, which satisfies $\mathrm{d}\eta \equiv \mathrm{d}t/a$. At sufficiently early times, when a given mode k is deep inside the Hubble horizon (i.e., $k \gg aH$), it is assumed to be in the Bunch-Davis vacuum state [56], which sets an initial condition for solving the Mukhanov-Sasaki equation:

$$v_k \to \frac{1}{\sqrt{2k}}\,\mathrm{e}^{-\mathrm{i}k\eta}, \quad k \gg aH. \tag{10}$$

After a period of inflation, this mode become super-Hubble, i.e., $k \ll aH$, and $|v_k|$ approaches a constant, which can be obtained by solving the Mukhanov-Sasaki equation. Then, the power spectrum can be expressed as

$$\mathcal{P}_\zeta(k) = \frac{k^3}{2\pi^2}\left|\frac{v_k}{z}\right|^2. \tag{11}$$

Calculating the power spectrum is the crucial first step for studying the production of SIGWs and PBHs, which we analyze in the subsequent sections.

III. SCALAR-INDUCED GRAVITATIONAL WAVES

During the radiation-dominated era, where the parameter for equation of state is $w = 1/3$, large scalar perturbations originating from inflation can source second-order GWs, known as SIGWs. In this section, we briefly review the formalism for the related calculation. We begin with the perturbed metric in the conformal Newtonian gauge, given by [57]

$$\mathrm{d}s^2 = a^2(\eta)\left\{-(1+2\Psi)\mathrm{d}\eta^2 + \left[(1-2\Psi)\delta_{ij} + \frac{h_{ij}}{2}\right]\mathrm{d}x^i\mathrm{d}x^j\right\}, \tag{12}$$

Here, $a(\eta)$ is the scale factor as a function of the conformal time η. We have neglected vector perturbations and anisotropic stress. This allows us to set two scalar Bardeen potentials equal: $\Phi = \Psi$. Thus, Ψ and h_{ij} represent the scalar and tensor perturbations, respectively.

To analyze the tensor perturbations, we expand h_{ij} in the Fourier space as

$$h_{ij}(\boldsymbol{x}, \eta) = \int \frac{\mathrm{d}^3 k\, \mathrm{e}^{\mathrm{i}\boldsymbol{k}\cdot\boldsymbol{x}}}{(2\pi)^{3/2}} [h^{+}_{\boldsymbol{k}}(\eta) e^{+}_{ij}(\boldsymbol{k}) + h^{\times}_{\boldsymbol{k}}(\eta) e^{\times}_{ij}(\boldsymbol{k})], \tag{13}$$

where polarization tensors $e^{+}_{ij}(\boldsymbol{k})$ and $e^{\times}_{ij}(\boldsymbol{k})$ correspond to the plus- and cross-polarization states, respectively. They are defined as

$$e^{+}_{ij}(\boldsymbol{k}) = \frac{1}{\sqrt{2}} \big[e_i(\boldsymbol{k})\, e_j(\boldsymbol{k}) - \tilde{e}_i(\boldsymbol{k})\, \tilde{e}_j(\boldsymbol{k}) \big], \tag{14}$$

$$e^{\times}_{ij}(\boldsymbol{k}) = \frac{1}{\sqrt{2}} \big[e_i(\boldsymbol{k})\, \tilde{e}_j(\boldsymbol{k}) + \tilde{e}_i(\boldsymbol{k})\, e_j(\boldsymbol{k}) \big], \tag{15}$$

where $e_i(\boldsymbol{k})$ and $\tilde{e}_i(\boldsymbol{k})$ are two mutually orthonormal basis vectors perpendicular to the wave vector $\boldsymbol{k}$.

The equation of motion for the Fourier modes of the tensor perturbations, $h^{\lambda}_{\boldsymbol{k}}$, sourced by scalar perturbations, is [12, 13]

$$h''_{\boldsymbol{k}}(\eta) + 2\mathcal{H} h'_{\boldsymbol{k}}(\eta) + k^2 h_{\boldsymbol{k}}(\eta) = 4 S_{\boldsymbol{k}}(\eta), \tag{16}$$

where $\mathcal{H} = a'/a$ is the conformal Hubble parameter. The source term $S_{\boldsymbol{k}}$ arises from the quadratic interactions of the linear scalar perturbations, given by [12, 13, 19]

$$\begin{aligned} S_{\boldsymbol{k}}(\eta) = \int & \frac{\mathrm{d}^3 \tilde{k}}{(2\pi)^{3/2}}\, e_{ij}(\boldsymbol{k}) \tilde{k}^i \tilde{k}^j \\ & \times \left\{ 2\Psi_{\tilde{\boldsymbol{k}}}(\eta) \Psi_{\boldsymbol{k}-\tilde{\boldsymbol{k}}}(\eta) + \frac{1}{\mathcal{H}^2} \left[\Psi'_{\tilde{\boldsymbol{k}}}(\eta) + \mathcal{H} \Psi_{\tilde{\boldsymbol{k}}}(\eta) \right] \left[\Psi'_{\boldsymbol{k}-\tilde{\boldsymbol{k}}}(\eta) + \mathcal{H} \Psi_{\boldsymbol{k}-\tilde{\boldsymbol{k}}}(\eta) \right] \right\}. \end{aligned} \tag{17}$$

During the radiation-dominated era, the Fourier modes of the Bardeen potential $\Psi_{\boldsymbol{k}}$ are related to the primordial curvature perturbations $\zeta_{\boldsymbol{k}}$, and generated during inflation via the transfer function $T(k\eta)$:

$$\Psi_{\boldsymbol{k}}(\eta) = \frac{2}{3}\, T(k\eta)\, \zeta_{\boldsymbol{k}}, \tag{18}$$

with

$$T(k\eta) = 3 \left[\frac{\sin\left(k\eta/\sqrt{3}\right) - \left(k\eta/\sqrt{3}\right) \cos\left(k\eta/\sqrt{3}\right)}{\left(k\eta/\sqrt{3}\right)^3} \right]. \tag{19}$$

The solution to Eq. (16) via the Green's function method is

$$h_{\boldsymbol{k}}(\eta) = \frac{4}{a(\eta)} \int_{\eta_i}^{\eta} \mathrm{d}\tilde{\eta}\, g_{\boldsymbol{k}}(\eta, \tilde{\eta}) a(\tilde{\eta}) S_{\boldsymbol{k}}(\tilde{\eta}). \tag{20}$$

Here, the Green's function $g_{\boldsymbol{k}}(\eta, \tilde{\eta})$ satisfies the equation of motion

$$g''_{\boldsymbol{k}}(\eta, \tilde{\eta}) + \left(k^2 - \frac{a''}{a} \right) g_{\boldsymbol{k}}(\eta, \tilde{\eta}) = \delta(\eta - \tilde{\eta}). \tag{21}$$

During the radiation-dominated era, the scale factor evolves as $a(\eta) \propto \eta$, which implies $a''/a = 0$. In this case, the above equation simplifies and the Green's function reads

$$g_{\boldsymbol{k}}(\eta, \tilde{\eta}) = \frac{\sin\left[k(\eta - \tilde{\eta})\right]}{k}. \tag{22}$$

The dimensionless power spectrum of tensor perturbations, $\mathcal{P}_h(k, \eta)$, is defined via the two-point correlation function of the Fourier modes $h_{\boldsymbol{k}}(\eta)$ as follows,

$$\langle h_{\boldsymbol{k}}(\eta) h_{\tilde{\boldsymbol{k}}}(\eta)\rangle \equiv \frac{2\pi^2}{k^3}\, \delta^{(3)}(\boldsymbol{k} + \tilde{\boldsymbol{k}}) \mathcal{P}_h(k, \eta). \tag{23}$$

Since the tensor perturbations are sourced by terms that are quadratic in the scalar perturbations, as seen from Eqs. (17), (18), and (20), their respective power spectra are related. Combining Eqs. (7) and (23), we find that the tensor power spectrum is proportional to the square of the scalar power spectrum:

$$\mathcal{P}_h(k, \eta) \propto \mathcal{P}_\zeta^2(k)\,. \tag{24}$$

The differential SIGW energy density corresponding to the tensor perturbations can be represented by the dimensionless quantity

$$\Omega_{\rm GW}(k, \eta) \equiv \frac{1}{\rho_{\rm c}} \frac{{\rm d}\rho_{\rm GW}}{{\rm d}\ln k} = \frac{1}{24} \left(\frac{k}{aH}\right)^2 \mathcal{P}_h(k, \eta), \tag{25}$$

where $\rho_{\rm c}$ is critical energy density. Since the tensor perturbations are sourced by the scalar perturbations, $\Omega_{\rm GW}$ can be computed directly from the primordial curvature power spectrum $\mathcal{P}_\zeta$. During the radiation-dominated era, this relation is given by the integral [19, 58]

$$\Omega_{\rm GW}(k, \eta) = \int_0^\infty {\rm d}v \int_{|1-v|}^{1+v} {\rm d}u\, \mathcal{T}(u, v) \mathcal{P}_\zeta(ku) \mathcal{P}_\zeta(kv), \tag{26}$$

where the integration variables are $u = |\boldsymbol{k} - \tilde{\boldsymbol{k}}|/k$ and $v = \tilde{k}/k$. The integration kernel $\mathcal{T}(u, v)$ is

$$\begin{aligned}\mathcal{T}(u, v) =& \frac{1}{12} \left[\frac{4v^2 - (1 - u^2 + v^2)^2}{4uv}\right]^2 \left[\frac{3(u^2 + v^2 - 3)}{4u^3 v^3}\right]^2 \\ &\times \left[\left(-4uv + (u^2 + v^2 - 3) \ln\left|\frac{3 - (u + v)^2}{3 - (u - v)^2}\right|\right)^2 + \pi^2 (u^2 + v^2 - 3)^2 \Theta(v + u - \sqrt{3})\right],\end{aligned} \tag{27}$$

where Θ denotes the Heaviside theta function.

Since the energy density of GWs evolves like radiation after their generation, the GW spectrum at the present time, $\Omega_{\rm GW}(k)$, is related to its value at formation, $\Omega_{\rm GW}(k, \eta)$, through

$$\Omega_{\rm GW}(k) h^2 = c_g \Omega_{\rm r,0} h^2 \Omega_{\rm GW}(k, \eta), \tag{28}$$

with $\Omega_{\rm r,0} h^2 \simeq 4.2 \times 10^{-5}$ representing the current energy density of radiation, where h is the Hubble constant in units of 100 $\mathrm{km\,s^{-1}\,Mpc^{-1}}$. The factor [59]

$$c_g = \frac{g_*}{g_*^0} \left(\frac{g_{*,s}^0}{g_{*,s}}\right)^{4/3} \tag{29}$$

accounts for the dependence on the effective relativistic degrees of freedom associated with energy and entropy, g_* and $g_{*,s}$. Assuming degrees of freedom in the standard model, one finds $g_* = g_{*,s} = 106.75$ at very early times in the radiation-dominated era, while their present values are $g_*^0 = 3.36$ and $g_{*,s}^0 = 3.91$. This leads to $c_g \simeq 0.39$.

IV. PRIMORDIAL BLACK HOLES

PBHs are usually characterized by their mass $M_{\rm PBH}$ and abundance $f_{\rm PBH}$. When sufficiently large curvature perturbations reenter the Hubble horizon during the radiation-dominated era, the self-gravity of the resulting overdense regions can overcome the opposing radiation pressure, causing them to collapse almost immediately into PBHs. The PBH mass $M_{\rm PBH}$ is set by the horizon mass $M_H = 4\pi\rho_{\rm tot}/(3H^3)$, where $\rho_{\rm tot}$ is the total energy density of the universe, at reentry [47, 60]:

$$M_{\rm PBH} = \gamma M_H = \gamma \frac{4\pi \cdot 3m_{\rm Pl}^2 H^2}{3H^3} = \frac{4\pi\gamma m_{\rm Pl}^2}{H}, \tag{30}$$

which can be expressed in terms of the comoving wavenumber k of the perturbation by [48]

$$M_{\rm PBH} \simeq M_\odot \frac{\gamma}{0.2}\left(\frac{g_*}{106.75}\right)^{-1/6}\left(\frac{k}{1.83\times10^6\ {\rm Mpc}^{-1}}\right)^{-2}. \tag{31}$$

Here, $\gamma \simeq 0.2$ is the collapse efficiency during the radiation-dominated era [9, 60, 61], and the effective relativistic degrees of freedom at PBH formation are taken to be $g_* = 106.75$.

The present mass fraction of PBHs in total dark matter (DM) is defined as $f_{\rm PBH}^{\rm tot} = \Omega_{\rm PBH}/\Omega_{\rm DM}$, where $\Omega_{\rm PBH}$ and $\Omega_{\rm DM}$ are the present energy densities of PBHs and DM, respectively, both normalized by the critical energy density $\rho_{\rm c}$. It can be expressed as an integral

$$f_{\rm PBH}^{\rm tot} = \int \frac{{\rm d}M_{\rm PBH}}{M_{\rm PBH}} f_{\rm PBH}(M_{\rm PBH}), \tag{32}$$

where the mass function of fractional PBH abundance is [60]

$$f_{\rm PBH}(M_{\rm PBH}) = \frac{1}{\Omega_{\rm DM}}\frac{{\rm d}\Omega_{\rm PBH}}{{\rm d}\ln M_{\rm PBH}} = 1.68\times10^8\left(\frac{\gamma}{0.2}\right)^{1/2}\left(\frac{g_*}{106.75}\right)^{-1/4}\left(\frac{M_{\rm PBH}}{M_\odot}\right)^{-1/2}\beta(M_{\rm PBH}). \tag{33}$$

Here, $M_\odot$ is the mass of the Sun, while $\beta(M_{\rm PBH})$ is the mass fraction of PBHs at formation, defined as

$$\beta(M_{\rm PBH}) = \left.\frac{\rho_{\rm PBH}}{\rho_{\rm tot}}\right|_{\rm formation}, \tag{34}$$

where $\rho_{\rm PBH}$ is the energy density of PBHs.

In the Press-Schechter formalism [62], $\beta(M_{\rm PBH})$ for a given PBH mass $M_{\rm PBH}$ is defined by the probability that the Gaussian density contrast (or equivalently, the Gaussian comoving curvature perturbation ζ or $\mathcal{R}$), coarse-grained over the comoving Hubble scale by a suitable window function, is larger than a threshold $\delta_{\rm th}$ for PBH formation. Therefore, it can be expressed as [16, 60, 61, 63]

$$\beta(M_{\rm PBH}) = \gamma\int_{\delta_{\rm th}}^1 \frac{{\rm d}\delta}{\sqrt{2\pi}\sigma_{M_{\rm PBH}}}\exp\left(-\frac{\delta^2}{2\sigma_{M_{\rm PBH}}^2}\right) \simeq \gamma\frac{\sigma_{M_{\rm PBH}}}{\sqrt{2\pi}\delta_{\rm th}}\exp\left(-\frac{\delta_{\rm th}^2}{2\sigma_{M_{\rm PBH}}^2}\right). \tag{35}$$

In our calculations, we adopt the threshold value to be $\delta_{\rm th} = 0.414$ [63]. The variance of the density contrast coarse-grained over the comoving Hubble scale $R = 1/k = 1/(aH)$ is [16]

$$\sigma^2_{M_{\rm PBH}} = \frac{16}{81}\int \frac{{\rm d}q}{q}\left(\frac{q}{k}\right)^4 W^2(q,R)\mathcal{P}_\zeta(q), \tag{36}$$

where $W(q,R)$ is the Fourier transform of the Gaussian window used to smooth the density contrast field on the scale R, given by [16, 61]

$$W(q,R) = \exp\left(-\frac{1}{2}q^2R^2\right). \tag{37}$$

Substituting this window function into Eq. (36), we arrive at

$$\sigma^2_{M_{\rm PBH}} = \frac{16}{81}\int \frac{{\rm d}q}{q}\left(\frac{q}{k}\right)^4 \exp\left(-\frac{q^2}{k^2}\right)\mathcal{P}_\zeta(q). \tag{38}$$

V. MODELS AND RESULTS

In this section, we consider a localized feature in a single-field inflationary potential that leads to an enhancement on the power spectrum of curvature perturbations. The potential can be expressed as [50]

$$V(\phi) = V_{\rm base}(\phi)\left[1 \pm \varepsilon(\phi)\right], \tag{39}$$

where $V_{\rm base}(\phi)$ is the base inflationary potential responsible for slow-roll inflation and generating primordial fluctuations compatible with the CMB constraints. The term $\varepsilon(\phi) \ll 1$ represents a small, localized correction to this potential. The "+" sign corresponds to a localized "bump" feature, while the "−" sign corresponds to a localized "dip" feature. We model $\varepsilon(\phi)$ as a Gaussian feature with height A, width σ, and centered at $\phi_{\rm d}$ [50, 64]:

$$\varepsilon(\phi) = A\exp\left[-\frac{1}{2}\frac{(\phi-\phi_{\rm d})^2}{\sigma^2}\right]. \tag{40}$$

We assume the base potential originated from string-theory-based KKLT inflation [51, 52, 65–68], which has a form of [68]

$$V_{\rm base}(\phi) = V_0\,\frac{\phi^n}{\phi^n + M^n}, \tag{41}$$

where V_0 fixes the overall CMB normalization. Although the base potential has two free parameters M and n, we shall set $M = m_{\rm Pl}/2$ and $n = 2$ for simplicity.

A. KKLT Inflation Featuring a Localized Bump in the Potential

When we add a bump feature by choosing the "+" sign in Eq. (39), the full potential in this bump scenario becomes

$$V(\phi) = V_0\,\frac{\phi^2}{M^2+\phi^2}\left\{1 + A\exp\left[-\frac{1}{2}\frac{(\phi-\phi_{\rm d})^2}{\sigma^2}\right]\right\}. \tag{42}$$

BPs	$V_0/m_{\rm Pl}^4$	A	$\phi_{\rm d}/m_{\rm Pl}$	$\sigma/m_{\rm Pl}$
B1	1.26473×10^{-10}	1.2025×10^{-3}	2.2049	1.67834×10^{-2}
B2	8.47671×10^{-11}	1.1701×10^{-3}	2.1881	1.58988×10^{-2}
B3	7.97916×10^{-11}	1.3888×10^{-3}	2.1111	1.70095×10^{-2}
B4	6.78765×10^{-11}	1.6888×10^{-3}	1.9999	1.74982×10^{-2}

TABLE I. Parameter values of four BPs in the bump scenario.

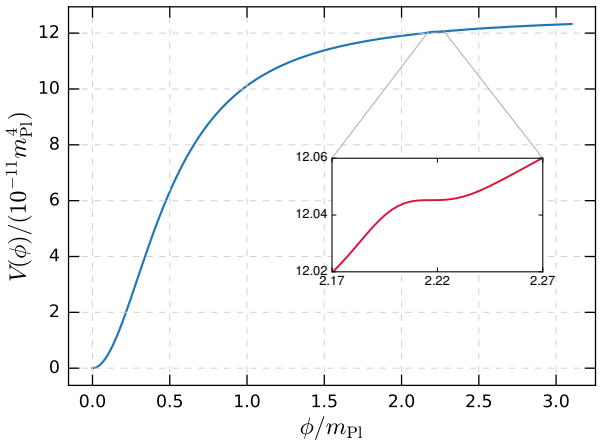

FIG. 1. KKLT potential with a localized small bump for BP B1.

The potential $V(\phi)$ depends on four parameters $\{V_0, A, \phi_{\rm d}, \sigma\}$. Because V_0 can be fixed by the CMB amplitude, the remaining three parameters $\{A, \phi_{\rm d}, \sigma\}$ essentially constitute the free parameter set in our analysis.

We adopt four benchmark points (BPs) in the parameter space, as listed in Table I. The BPs have been chosen such that the resulting SIGWs are detectable within the sensitive frequency bands of current and future GW experiments. The bumps in the potential for these BPs are extremely small, since the parameter $A \ll 1$. In Figure 1, we demonstrate the potential as a function of ϕ for BP B1, where the bump feature is highlighted in the inset, which provides a greatly magnified view.

1. *Primordial Curvature Power Spectrum*

A large amplification of the primordial curvature power spectrum $\mathcal{P}_\zeta$ is obtained by slowing down the inflaton field with the bump feature in the potential. To compute the power spectrum, we first solve the set of cosmological equations (2) with the potential (42) for the background evolution. Using BP B1 as an example, Figure 2 shows the resulting evolution of the inflaton field ϕ and the Hubble parameter H as functions of the number of e-folds $N - N_{\rm end}$, where $N_{\rm end}$ denotes the e-folding number at the end of inflation. The plateaus in the ϕ and H curves between $N - N_{\rm end} \sim -40$ to ~ -26 arise from the bump feature, which causes a temporary deceleration, briefly interrupting the slow-roll evolution. In Figure 3, we demonstrate the evolution of the slow-

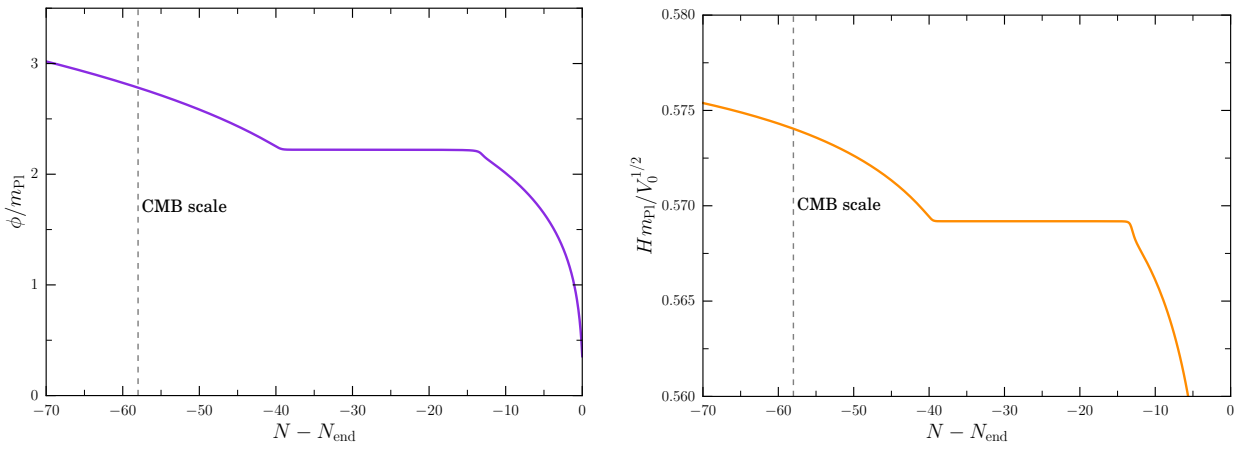

(a) Inflaton field (b) Hubble parameter

FIG. 2. Evolution of the inflaton field ϕ (a) and the Hubble parameter H (b) as functions the number of e-folds $N - N_{\rm end}$ for BP B1.

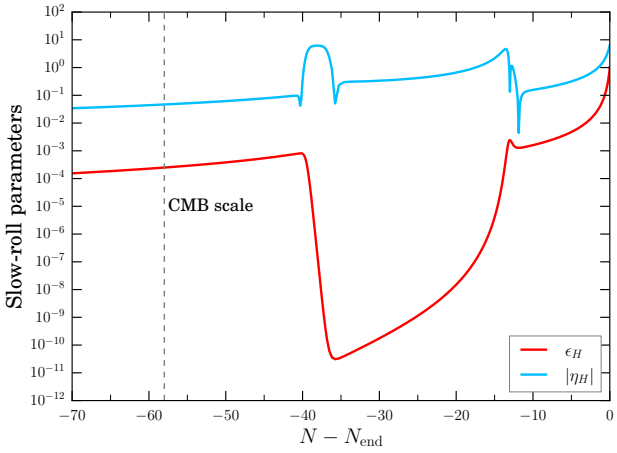

FIG. 3. Evolution of the slow-roll parameters ϵ_H and η_H as functions the number of e-folds $N - N_{\rm end}$ for BP B1.

roll parameters ϵ_H and η_H. The deceleration effect is clearly reflected in the sharp drop of ϵ_H over the interval $-40 \lesssim N - N_{\rm end} \lesssim -26$.

This background evolution is then used as input for the Mukhanov-Sasaki equation (9), which is solved to obtain the curvature power spectrum $\mathcal{P}_\zeta$. The resulting power spectrum is shown as the blue line in Figure 4 for BP B1, where the value of the parameter V_0 has been calibrated to match the CMB observation of the amplitude at the CMB pivot scale. We employ the full Mukhanov-Sasaki equation (9) over the slow-roll approximation (8), because the latter significantly underestimates the overall amplitude of the power spectrum, as demonstrated in Figure 4.

Furthermore, we display the primordial curvature power spectra $\mathcal{P}_\zeta$ as functions of the comoving wavenumber k for the four BPs from Table I in Figure 5. All four spectra satisfy the CMB normalization condition, $\mathcal{P}_\zeta(k_*) = 2.1 \times 10^{-9}$ at the pivot scale $k_* = 0.05$ Mpc^{-1} [5], to match the

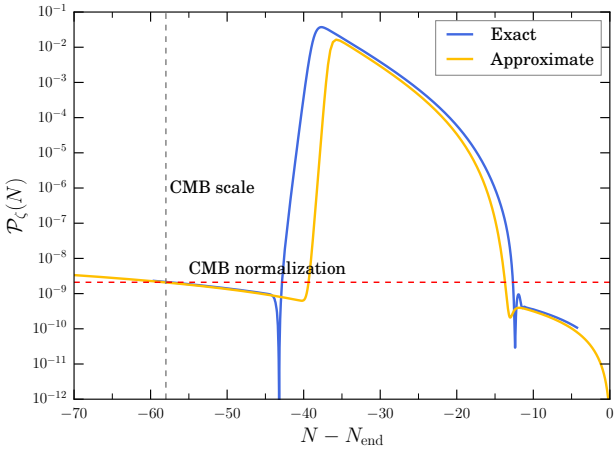

FIG. 4. Primordial curvature power spectrum $\mathcal{P}_\zeta$ as a function of the e-folding number for BP B1 obtained by exactly solving the Mukhanov-Sasaki equation (blue line), compared to that given by the slow-roll approximation (yellow line).

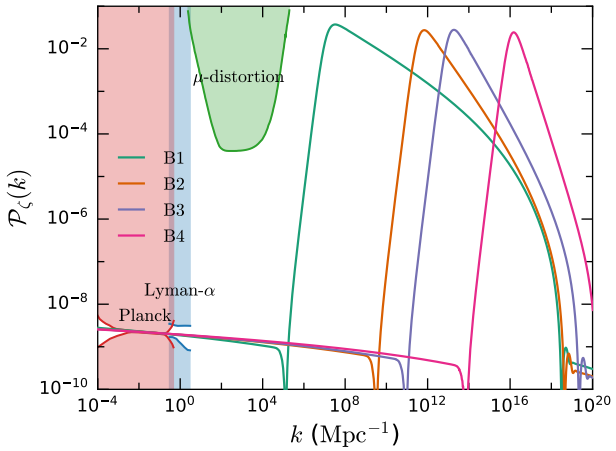

FIG. 5. Primordial curvature power spectra as functions of the comoving wavenumber k for BP B1 (green line), B2 (orange line), B3 (purple line), and B4 (magenta line). The red-, blue-, and green-shaded regions are excluded by the Planck CMB observations [72], the Lyman-α forest [69], and the μ-distortion of CMB [70].

observation. The constraints from the Lyman-α forest [69] and the CMB μ-distortion [70] are also shown in the figure, which is generated using the `PBHbounds` code [71]. The power spectra for the four BPs reach peak amplitudes $\mathcal{P}_\zeta \sim 10^{-2}$ at different scales. The features are listed below.

- **BP B1:** the enhancement begins at $k \sim 10^5$ Mpc^{-1} and peaks at $k \sim 10^7$ Mpc^{-1}.
- **BP B2:** the enhancement begins at $k \sim 10^9$ Mpc^{-1} and peaks at $k \sim 10^{12}$ Mpc^{-1}.
- **BP B3:** the enhancement begins at $k \sim 10^{11}$ Mpc^{-1} and peaks at $k \sim 10^{13}$ Mpc^{-1}.
- **BP B4:** the enhancement begins at $k \sim 10^{14}$ Mpc^{-1} and peaks at $k \sim 10^{16}$ Mpc^{-1}.

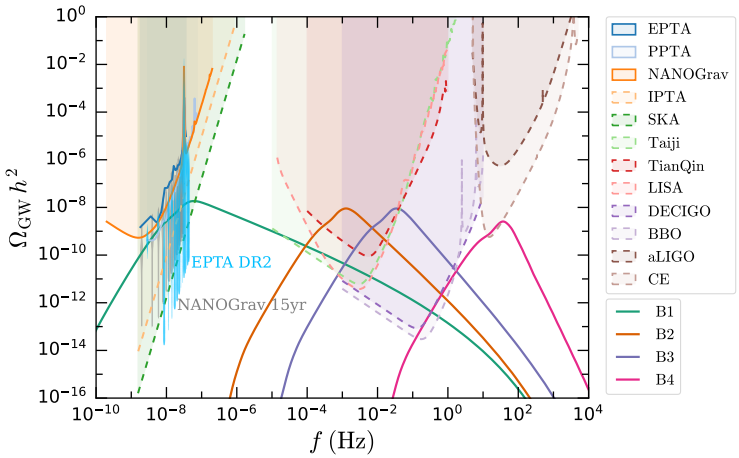

FIG. 6. Predicted SIGW spectra $\Omega_{\rm GW}h^2$ for BP B1 (green line), B2 (orange line), B3 (purple line), and B4 (magenta line). For comparison, exclusion limits from current GW experiments (solid lines) and sensitivity curves of future GW observatories (dashed lines) are also shown, including EPTA [73], PPTA [74], NANOGrav [75], IPTA [76], SKA [76], LISA [77], Taiji [78], TianQin [79], DECIGO [80], BBO [81], aLIGO [82], and CE [83]. Gray and cyan violins represent the posterior distributions corresponding to evidence of an SGWB observed in the NANOGrav 15-yr [84] and EPTA DR2 [41, 85] datasets.

2. *Scalar-induced Gravitational Waves*

A significant amplification of the primordial curvature power spectrum, caused by the bump feature, could produce a prominent stochastic SIGW background. To calculate the present-day energy density of SIGWs, we first substitute the power spectrum $\mathcal{P}_\zeta(k)$ into Eq. (26) to derive the GW energy density at the time of generation during the radiation-dominated era, $\Omega_{\rm GW}(k,\eta)$. The result is subsequently evolved to its present value using the relation in Eq. (28). Applying this procedure to the primordial curvature power spectra shown in Figure 5, we obtain the SIGW energy density spectra $\Omega_{\rm GW}h^2$ for the four BPs, as plotted in Figure 6.

For comparison, in Figure 6 we also demonstrate the existed exclusion limits from PTA experiments EPTA [73], PPTA [74], and NANOGrav [75], as well as the sensitivity curves of future PTA experiments IPTA [76] and SKA [76], which cover the 10^{-9}–10^{-6} Hz frequency band. In the 10^{-5}–10 Hz band, the sensitivity curves of future space-borne laser interferometers LISA [77], TianQin [79], Taiji [78], DECIGO [80], and BBO [81] are plotted. Furthermore, we illustrate the sensitivity curves of future ground-based interferometers aLIGO [82] and CE [83], which search for GWs in the 10–10^3 Hz range. In addition, the gray and cyan violins in Figure 6 denote the posterior distributions by reconstructing an SGWB signal from the NANOGrav 15-yr [84] and EPTA DR2 [41, 85] dataset.

The peak frequency of the SIGW spectra is positively correlated to the peak comoving wavenumber of the primordial curvature power spectrum. Consequently, the SIGW spectra for the four BPs reach peak amplitudes of $\Omega_{\rm GW}h^2 \sim 10^{-8}$ at different frequencies with the following characteristics.

- **BP B1:** the SIGW spectrum peaks at a frequency of $f \sim 10^{-7}$ Hz, and it is in good agreement

with the posterior distributions for an SGWB in the frequency range 10^{-9}–10^{-7} Hz reported by NANOGrav and EPTA.

- **BP B2:** the SIGW spectrum peaks at a frequency of $f \sim 10^{-3}$ Hz and it is promising to be probed by LISA, TianQin, and Taiji.

- **BP B3:** the SIGW spectrum peaks at a frequency of $f \sim 10^{-1}$ Hz, falling into the sensitive bands of LISA, TianQin, Taiji, BBO, and DECIGO.

- **BP B4:** the SIGW spectrum peaks at a frequency of $f \sim 10$ Hz, which may be detected by CE.

3. Primordial Black Holes

Beyond sourcing SIGWs, the enhanced primordial curvature power spectrum also drives a substantial production of PBHs. The procedure to evaluate their abundance is as follows. First, the power spectrum $\mathcal{P}_\zeta(k)$ is used to compute the variance of the density contrast via Eq. (38). This variance is then substituted into Eq. (35) to determine the initial mass fraction of PBHs, $\beta(M_{\rm PBH})$. The PBH mass $M_{\rm PBH}$ is related to the comoving wavenumber k through Eq. (31). Finally, the present-day fractional abundance of PBHs in total DM, $f_{\rm PBH}(M_{\rm PBH})$, is calculated using Eq. (33).

A key parameter in this calculation is the density threshold for collapse, $\delta_{\rm th}$. In our analysis, we adopt the value $\delta_{\rm th} = 0.414$ [63]. Nevertheless, It is important to note that detailed analytical and numerical investigations suggest a rather broad possible range for this threshold, from 0.3 to 0.66, for PBH formation in the radiation-dominated era [8, 63, 86–91]. A smaller value of $\delta_{\rm th}$ results in a larger PBH abundance.

Furthermore, the PBH abundance $f_{\rm PBH}$ is highly sensitive to the peak amplitude of the primordial curvature power spectrum $\mathcal{P}_\zeta$. This sensitivity arises because the abundance depends exponentially on the variance of the density contrast, $\sigma_{M_{\rm PBH}}$, which is in turn computed from $\mathcal{P}_\zeta$. Consequently, generating a significant PBH abundance at a specific mass scale demands that the inflationary potential parameters are highly fine-tuned, typically to several decimal places. We emphasize that this fine-tuning is a generic feature of PBH formation from a narrow spectral peak and not a peculiarity of the specific inflationary model considered here, as pointed out in Refs. [48, 49].

For the four BPs, we estimate the resulting PBH fractional abundances, which have the following characteristics.

- **BP B1:** $M_{\rm PBH} \sim 3 \times 10^{-3} M_\odot$ with $f_{\rm PBH} \sim 5.8 \times 10^{-4}$.

- **BP B2:** $M_{\rm PBH} \sim 10^{-11} M_\odot$ with $f_{\rm PBH} \sim 2.4 \times 10^{-4}$.

- **BP B3:** $M_{\rm PBH} \sim 10^{-14} M_\odot$ with $f_{\rm PBH} \sim 7.1 \times 10^{-3}$.

- **BP B4:** $M_{\rm PBH} \sim 1.3 \times 10^{-20} M_\odot$ with $f_{\rm PBH} \sim 10^{-13}$.

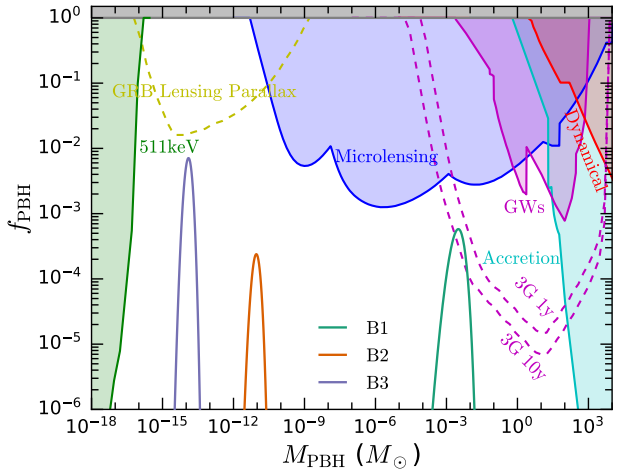

FIG. 7. Fractional abundances of PBHs at the present for BP B1 (green line), B2 (orange line), and B3 (purple line). Colored shaded regions are excluded by various existed constraints arising from the 511 keV line (green) [92], microlensing (blue) [93–102], gravitational waves (magenta) [103–107], accretion (light blue) [108–111], and dynamical effects (red) [112, 113]. The dashed lines show projected constraints from future observations, including third-generation ground-based GW detectors with 1 and 10 years of observation (magenta) [114] and the lensing parallax of γ-ray bursts (yellow) [115].

Note that the peak PBH mass is negatively correlated to the peak comoving wavenumber of the primordial curvature power spectrum, as specified in Eq. (31). The results for BP B1, B2, and B3 are plotted in Figure 7.

Constraints on the fractional abundance of PBHs are derived from a variety of astrophysical and cosmological observations. These constraints arise from several processes, such as evaporation, gravitational lensing, dynamical interactions, accretion, and GW emissions. Evaporation limits come from the extragalactic γ-ray background (EGB) [116], CMB anisotropies [117], the Galactic γ-ray background (GGB) [118], the cosmic X-ray background [92, 119], Voyager-1 $e^{\pm}$ [120], the EDGES 21 cm line [121], and the 511 keV line [92]. Lensing constraints originate from microlensing of stars in the M31 galaxy by Subaru [97], in the Magellanic Clouds by MACHO [96] and EROS [98], in the local neighborhood by Kepler [122], and in the Galactic bulge by OGLE [93, 94]. Dynamical limits are given by disruption of wide binaries [112] and the survival of the star clusters in Eridanus II and compact ultra-faint dwarf galaxies [113]. Accretion limits come from X-ray binaries [108], CMB anisotropies measured by Planck [109], and GWs from binary coalescences [103, 104]. The relevant constraints are also displayed in Figure 7, with the help of the `PBHbounds` code [71]. The PBH fractional abundances predicted by BP B1, B2, and B3 are consistent with all these bounds.

Furthermore, the dashed lines in Figure 7 demonstrate projected constraints from future experiments, including third-generation ground-based GW detectors [114] and the lensing parallax of γ-ray bursts (GRB) [115]. It shows that a third-generation GW observatory, with a decade of observation, can probe the PBH abundance projected by BP B1.

Because of Hawking radiation [125], PBHs with masses below $5 \times 10^{-19}\ M_\odot$ have completely evaporated before the present day and therefore do not contribute to the present DM energy density

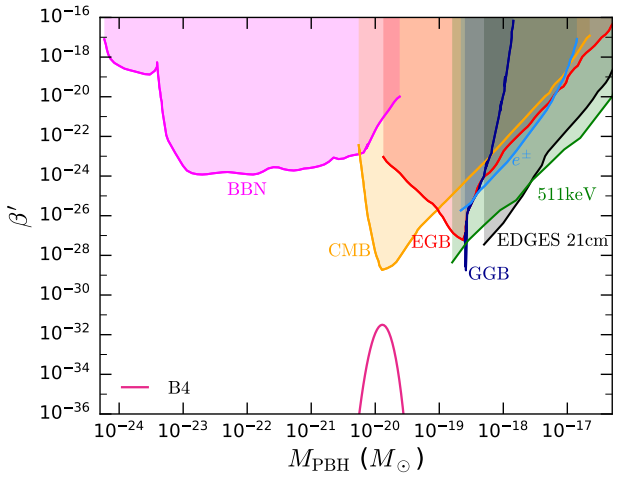

FIG. 8. Mass fraction of PBHs at formation for BP B4 (magenta line). Colored shaded regions are excluded by various observations, including big bang nucleosynthesis (pink) [123], extragalactic γ-ray background (red) [116], CMB spectral anisotropies (yellow) [124], Galactic γ-ray background (dark blue) [118], electrons and positrons observed by Voyager 1 (light blue) [120], the 21 cm line measurements from EDGES (black) [121], and the 511 keV line (green) [92].

[116, 123]. Since BP B4 predicts PBH masses around $1.3 \times 10^{-20} M_\odot$, the present-day fractional abundance $f_{\rm PBH}$ is meaningless. Nonetheless, such PBHs exist in the early universe, and we can characterize their abundance by the mass fraction $\beta(M_{\rm PBH})$ at formation, defined by Eq. (34). Since $\beta(M_{\rm PBH})$ always appears in combination with a factor of $\gamma^{1/2} g_*^{-1/4}$, it is convenient to introduce a rescaled quantity [116, 123]

$$\beta'(M_{\rm PBH}) \equiv \gamma^{1/2} \left(\frac{g_*}{106.75}\right)^{-1/4} \beta(M_{\rm PBH}). \tag{43}$$

The $\beta'(M_{\rm PBH})$ distribution for BP B4 is illustrated in Figure 8, where the constraints from EGB, CMB, GGB, electrons and positrons observed by Voyager 1, the 21 cm line, and the 511 keV line are also shown. Moreover, PBH evaporation at the epoch of big bang nucleosynthesis (BBN) would significantly alter the abundances of synthesized light elements. This leads to an important bound for $M_{\rm PBH} \lesssim 10^{-20} M_\odot$ [123], which is also plotted in Figure 8. Nonetheless, the PBH abundance predicted by BP B4 is sufficiently low to evade these constraints.

B. KKLT Inflation Featuring a Localized Dip in the Potential

In this subsection, we discuss a dip feature in the single-field inflationary potential, corresponding to the "−" sign in Eq. (39). The full potential this dip scenario becomes

$$V(\phi) = V_0 \frac{\phi^2}{M^2 + \phi^2} \left[1 - A \exp\left(-\frac{1}{2}\frac{(\phi - \phi_d)^2}{\sigma^2}\right)\right]. \tag{44}$$

Similar to the bump scenario, we fix the parameter V_0 via the CMB normalization, so that only three parameters, A, $\phi_{\rm d}$, and σ, remain free in the analysis. For the dip scenario, we also consider

BPs	$V_0/m_{\rm Pl}^4$	A	$\phi_{\rm d}/m_{\rm Pl}$	$\sigma/m_{\rm Pl}$
D1	1.22997×10^{-10}	2.2222×10^{-3}	2.2099	2.93035×10^{-2}
D2	8.49752×10^{-11}	2.2025×10^{-3}	2.1755	2.74165×10^{-2}
D3	7.59642×10^{-11}	2.3888×10^{-3}	2.1222	2.72462×10^{-2}
D4	6.62707×10^{-11}	2.8888×10^{-3}	2.0111	2.68766×10^{-2}

TABLE II. Parameter values of four BPs in the dip scenario.

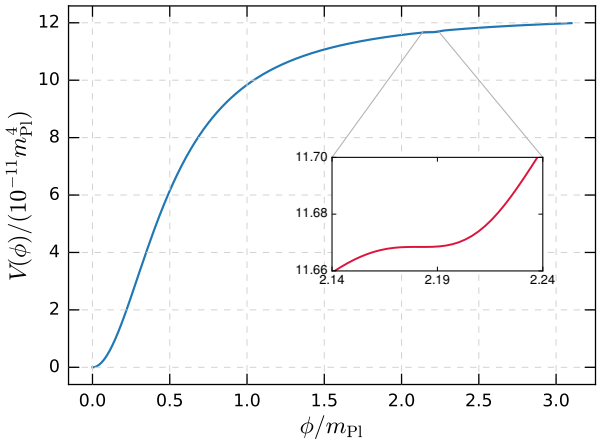

FIG. 9. KKLT potential with a localized small dip for BP D1.

four BPs in the parameter space, as tabulated in Table II. These BPs would leads to SIGWs at various frequency bands that could be probed by current and future GW experiments. As an illustrative example, the potential for BP D1 is plotted in Figure 9, where the inset highlight the dip feature.

1. *Primordial Curvature Power Spectrum*

After numerically solving the Mukhanov-Sasaki equation (9), we obtain the primordial curvature power spectra for the four BPs in the dip scenario, as shown in Figure 10. All of them are normalized to satisfy the CMB observation at the pivot scale.

For the four BPs, the power spectra exhibit peaks with amplitudes $\mathcal{P}_\zeta \sim 10^{-2}$, spanning different scales as detailed below.

- **BP D1:** the enhancement begins at $k \sim 10^5$ Mpc^{-1} and peaks at $k \sim 10^7$ Mpc^{-1}.
- **BP D2:** the enhancement begins at $k \sim 10^9$ Mpc^{-1} and peaks at $k \sim 10^{12}$ Mpc^{-1}.
- **BP D3:** the enhancement begins at $k \sim 10^{12}$ Mpc^{-1} and peaks at $k \sim 10^{14}$ Mpc^{-1}.
- **BP D4:** the enhancement begins at $k \sim 10^{14}$ Mpc^{-1} and peaks at $k \sim 10^{16}$ Mpc^{-1}.

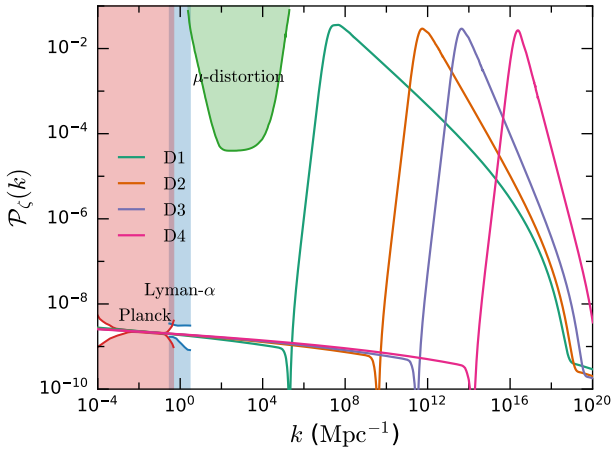

FIG. 10. Primordial curvature power spectra as functions of the comoving wave number for BP D1 (green line), D2 (orange line), D3 (purple line), and D4 (magenta line). The shaded regions have the same meanings as in Figure 5.

These behaviors are analogous to those of the BPs in the bump scenario, because a dip feature in the potential also leads to a temporary deceleration of the slow-roll evolution, just like a bump feature.

Nevertheless, the two scenarios differ in the relative positions of $k(\phi_{\rm d})$ and $k_{\rm peak}$, where $k(\phi_{\rm d})$ is the comoving wavenumber corresponding to the bump/dip center $\phi_{\rm d}$ and $k_{\rm peak}$ is the peak comoving wavenumber of the curvature power spectrum. In the bump scenario, $k(\phi_{\rm d})$ lies to the right of $k_{\rm peak}$, i.e., $k_{\rm peak} < k(\phi_{\rm d})$, whereas in the dip scenario, it lies to the left of $k_{\rm peak}$, i.e., $k_{\rm peak} > k(\phi_{\rm d})$. The physical reason for this shift is that the enhancement of $\mathcal{P}_\zeta$ is driven by the temporary deceleration as the inflaton field "climbs" the localized feature of the potential. For a bump, this climbing phase occurs as the field approaches the peak at $\phi_{\rm d}$ from below. In contrast, for a dip, the field decelerates as it climbs out of the feature after passing the minimum at $\phi_{\rm d}$.

2. *Scalar-induced Gravitational Waves*

Using the small-scale enhanced power spectra shown in Figure 10, we compute the corresponding SIGW energy density spectra, $\Omega_{\rm GW}h^2$, which are plotted in Figure 11. The SIGW spectra for the four BPs achieve peak amplitudes of $\Omega_{\rm GW}h^2 \sim 10^{-8}$ at diverse frequencies, as featured below.

- **BP D1:** $\Omega_{\rm GW}h^2$ peaks at $f \sim 10^{-7}$ Hz. This SIGW spectrum agrees well with the evidence for an SGWB from the NANOGrav and EPTA datasets released in 2023.

- **BP D2:** $\Omega_{\rm GW}h^2$ peaks at $f \sim 10^{-3}$ Hz, and it could be detected in future space-borne GW interferometers.

- **BP D3:** $\Omega_{\rm GW}h^2$ peaks at $f \sim 10^{-1}$ Hz, and it could also be probed by future space-borne GW experiments.

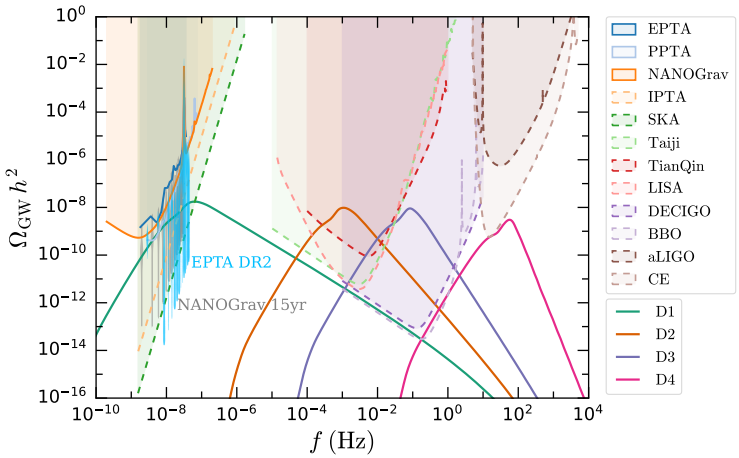

FIG. 11. Predicted SIGW spectra for BP D1 (green line), D2 (orange line), D3 (purple line), and D4 (magenta line). The remaining features in the figure are similar to those in Figure 6.

- **BP D4:** $\Omega_{\rm GW}h^2$ peaks at $f \sim 10^2$ Hz, and this signal would be accessible to a third-generation ground-based observatory like CE.

Despite the different underlying potential features, these SIGW spectra are qualitatively similar to those from the bump scenario.

3. Primordial black holes

The large amplifications of the primordial curvature power spectra for the four BPs result in a significant production of PBHs. In Fig. 12(a), we display the present-day fractional abundance of PBHs predicted by BP D1, D2, and D3, whose features are listed below.

- **BP D1:** $M_{\rm PBH} \sim 2.7 \times 10^{-3} M_\odot$ with $f_{\rm PBH} \sim 3.5 \times 10^{-4}$.
- **BP D2:** $M_{\rm PBH} \sim 1.2 \times 10^{-11} M_\odot$ with $f_{\rm PBH} \sim 6.4 \times 10^{-4}$.
- **BP D3:** $M_{\rm PBH} \sim 2.3 \times 10^{-15} M_\odot$ with $f_{\rm PBH} \sim 6.4 \times 10^{-3}$.

Besides, BP D4 predicts PBH production with $M_{\rm PBH} \sim 6.4 \times 10^{-21} M_\odot$. these PBHs evaporate via Hawking radiation and cannot survive to the present day. Their mass fraction at formation is demonstrated in Fig. 12(b).

VI. CONCLUSIONS AND DISCUSSIONS

In this work, we investigate the production of scalar-induced gravitational waves and primordial black holes arising from the inclusion of a localized bump/dip feature in the inflationary potential based on the string-theory-inspired KKLT model. Either a bump or dip feature can briefly decelerate the slow-roll evolution, leading to a large amplification of the primordial curvature power spectrum. Consequently, this amplification drives substantial emissions of SIGWs and production of PBHs.

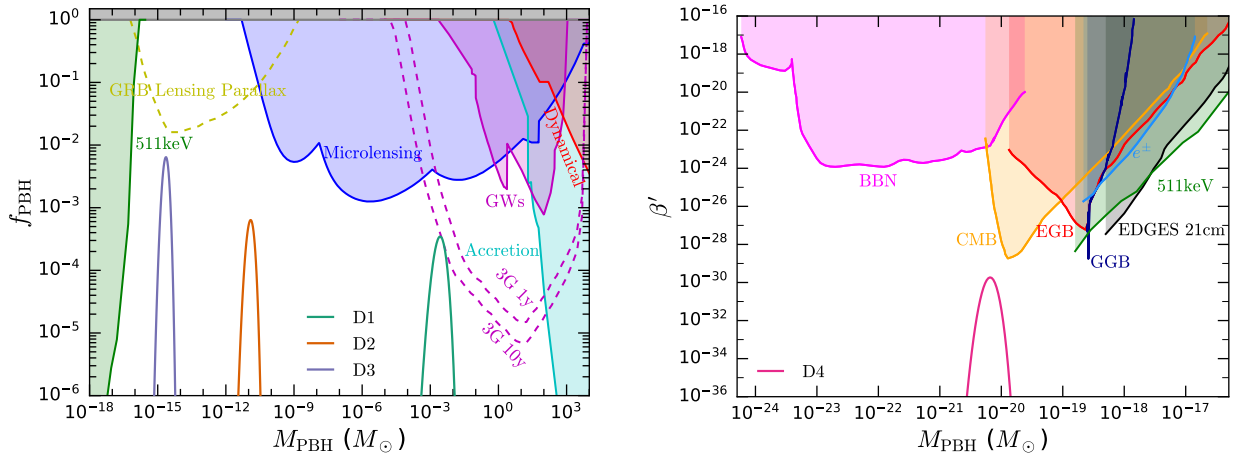

(a) $f_{\rm PBH}(M_{\rm PBH})$ distribution

(b) $\beta'(M_{\rm PBH})$ distribution

FIG. 12. Fractional abundances of PBHs at the present (a) for BP D1 (green line), D2 (orange line), and D3 (purple line), and the mass fraction of PBHs at formation (b) for BP D4 (magenta line). The remaining features in these plots are essentially the same as those already shown in Figure 7 and Figure 8.

By analyzing eight benchmark cases, four for the bump scenario and four for the dip scenario, we have detailed the resulting primordial curvature power spectra, SIGW spectra, and PBH abundances. Our results demonstrate that such a simple modification to the potential can effectively amplify the curvature power spectrum by approximately seven orders of magnitude at small scales. This enhancement is sufficient to produce a significant abundance of PBHs and to source a stochastic background of SIGWs, which is detectable by future GW experiments. The eight BPs yield PBHs of different masses and SIGW spectra that peak in various frequency bands, falling within the sensitivity ranges of diverse GW experiments, including PTAs, space-borne interferometers, and ground-based interferometers. Notably, the SIGW signals for BP B1 in the bump scenario and BP D1 in the dip scenario are consistent with the evidence for an SGWB reported by the PTA experiments in 2023.

Our analysis illustrates that a well-motivated inflationary model with a simple modification can simultaneously account for the origin of PBHs, which could constitute a substantial fraction of DM, and the plausible SGWB signal observed by PTAs in 2023. For this purpose, both the bump and dip scenarios produce comparable outcomes. Nonetheless, we acknowledge the challenges faced by this framework. Similar to many models of this type, achieving the desired enhancement requires a degree of fine-tuning of the model parameters. Furthermore, the final PBH abundance is highly sensitive to the choice of the collapse threshold $\delta_{\rm th}$, which remains subject to considerable theoretical uncertainties.

In summary, our work provides a concrete example of how inflationary dynamics can connect the physics of the early Universe with future multi-messenger astronomical observations. In the near future, more precise searches for both PBHs and GWs across multiple frequency bands could provide crucial tests for this class of models.

ACKNOWLEDGMENTS

This work is supported by the National Natural Science Foundation of China under Grant No. 12575115.

---

[1] A. H. Guth, "The Inflationary Universe: A Possible Solution to the Horizon and Flatness Problems," *Phys. Rev. D* **23** (1981) 347–356.

[2] A. D. Linde, "A New Inflationary Universe Scenario: A Possible Solution of the Horizon, Flatness, Homogeneity, Isotropy and Primordial Monopole Problems," *Phys. Lett. B* **108** (1982) 389–393.

[3] A. A. Starobinsky, "A New Type of Isotropic Cosmological Models Without Singularity," *Phys. Lett. B* **91** (1980) 99–102.

[4] A. Albrecht and P. J. Steinhardt, "Cosmology for Grand Unified Theories with Radiatively Induced Symmetry Breaking," *Phys. Rev. Lett.* **48** (1982) 1220–1223.

[5] **Planck** Collaboration, N. Aghanim *et al.*, "Planck 2018 results. VI. Cosmological parameters," *Astron. Astrophys.* **641** (2020) A6, arXiv:1807.06209 [astro-ph.CO]. [Erratum: Astron.Astrophys. 652, C4 (2021)].

[6] Y. B. Zel'dovich and I. D. Novikov, "The Hypothesis of Cores Retarded during Expansion and the Hot Cosmological Model," *Sov. Astron.* **10** (1967) 602.

[7] S. Hawking, "Gravitationally collapsed objects of very low mass," *Mon. Not. Roy. Astron. Soc.* **152** (1971) 75.

[8] B. J. Carr and S. W. Hawking, "Black holes in the early Universe," *Mon. Not. Roy. Astron. Soc.* **168** (1974) 399–415.

[9] B. J. Carr, "The Primordial black hole mass spectrum," *Astrophys. J.* **201** (1975) 1–19.

[10] M. Y. Khlopov, "Primordial Black Holes," *Res. Astron. Astrophys.* **10** (2010) 495–528, arXiv:0801.0116 [astro-ph].

[11] K. Tomita, "Non-Linear Theory of Gravitational Instability in the Expanding Universe," *Prog. Theor. Phys.* **37** (1967) 831–846.

[12] K. N. Ananda, C. Clarkson, and D. Wands, "The Cosmological gravitational wave background from primordial density perturbations," *Phys. Rev. D* **75** (2007) 123518, arXiv:gr-qc/0612013.

[13] D. Baumann, P. J. Steinhardt, K. Takahashi, and K. Ichiki, "Gravitational Wave Spectrum Induced by Primordial Scalar Perturbations," *Phys. Rev. D* **76** (2007) 084019, arXiv:hep-th/0703290.

[14] R. Saito and J. Yokoyama, "Gravitational wave background as a probe of the primordial black hole abundance," *Phys. Rev. Lett.* **102** (2009) 161101, arXiv:0812.4339 [astro-ph]. [Erratum: Phys.Rev.Lett. 107, 069901 (2011)].

[15] L. Alabidi, K. Kohri, M. Sasaki, and Y. Sendouda, "Observable Spectra of Induced Gravitational Waves from Inflation," *JCAP* **09** (2012) 017, arXiv:1203.4663 [astro-ph.CO].

[16] S. Young, C. T. Byrnes, and M. Sasaki, "Calculating the mass fraction of primordial black holes," *JCAP* **07** (2014) 045, arXiv:1405.7023 [gr-qc].

[17] T. Nakama, J. Silk, and M. Kamionkowski, "Stochastic gravitational waves associated with the formation of primordial black holes," *Phys. Rev. D* **95** (2017) 043511, arXiv:1612.06264 [astro-ph.CO].

[18] S.-L. Cheng, W. Lee, and K.-W. Ng, "Primordial black holes and associated gravitational waves in axion monodromy inflation," *JCAP* **07** (2018) 001, arXiv:1801.09050 [astro-ph.CO].

[19] K. Kohri and T. Terada, "Semianalytic calculation of gravitational wave spectrum nonlinearly

induced from primordial curvature perturbations," *Phys. Rev. D* **97** (2018) 123532, arXiv:1804.08577 [gr-qc].

[20] R.-G. Cai, Z.-K. Guo, J. Liu, L. Liu, and X.-Y. Yang, "Primordial black holes and gravitational waves from parametric amplification of curvature perturbations," *JCAP* **06** (2020) 013, arXiv:1912.10437 [astro-ph.CO].

[21] R.-g. Cai, S. Pi, and M. Sasaki, "Gravitational Waves Induced by non-Gaussian Scalar Perturbations," *Phys. Rev. Lett.* **122** (2019) 201101, arXiv:1810.11000 [astro-ph.CO].

[22] R.-G. Cai, S. Pi, S.-J. Wang, and X.-Y. Yang, "Pulsar Timing Array Constraints on the Induced Gravitational Waves," *JCAP* **10** (2019) 059, arXiv:1907.06372 [astro-ph.CO].

[23] C. Yuan, Z.-C. Chen, and Q.-G. Huang, "Probing primordial–black-hole dark matter with scalar induced gravitational waves," *Phys. Rev. D* **100** (2019) 8, arXiv:1906.11549 [astro-ph.CO].

[24] Z.-C. Chen, C. Yuan, and Q.-G. Huang, "Pulsar Timing Array Constraints on Primordial Black Holes with NANOGrav 11-Year Dataset," *Phys. Rev. Lett.* **124** (2020) 25, arXiv:1910.12239 [astro-ph.CO].

[25] S. Pi and M. Sasaki, "Gravitational Waves Induced by Scalar Perturbations with a Lognormal Peak," *JCAP* **09** (2020) 037, arXiv:2005.12306 [gr-qc].

[26] C. Yuan, Z.-C. Chen, and Q.-G. Huang, "Log-dependent slope of scalar induced gravitational waves in the infrared regions," *Phys. Rev. D* **101** (2020) 4, arXiv:1910.09099 [astro-ph.CO].

[27] C. Yuan, Z.-C. Chen, and Q.-G. Huang, "Scalar Induced Gravitational Waves in Different Gauges," *Phys. Rev. D* **101** (2020) 6, arXiv:1912.00885 [astro-ph.CO].

[28] G. Domènech, S. Pi, and M. Sasaki, "Induced gravitational waves as a probe of thermal history of the universe," *JCAP* **08** (2020) 017, arXiv:2005.12314 [gr-qc].

[29] R.-G. Cai, Y.-C. Ding, X.-Y. Yang, and Y.-F. Zhou, "Constraints on a mixed model of dark matter particles and primordial black holes from the galactic 511 keV line," *JCAP* **03** (2021) 057, arXiv:2007.11804 [astro-ph.CO].

[30] L. Liu, X.-Y. Yang, Z.-K. Guo, and R.-G. Cai, "Testing primordial black hole and measuring the Hubble constant with multiband gravitational-wave observations," *JCAP* **01** (2023) 006, arXiv:2112.05473 [astro-ph.CO].

[31] T. Papanikolaou, C. Tzerefos, S. Basilakos, and E. N. Saridakis, "Scalar induced gravitational waves from primordial black hole Poisson fluctuations in f(R) gravity," *JCAP* **10** (2022) 013, arXiv:2112.15059 [astro-ph.CO].

[32] T. Papanikolaou, C. Tzerefos, S. Basilakos, and E. N. Saridakis, "No constraints for f(T) gravity from gravitational waves induced from primordial black hole fluctuations," *Eur. Phys. J. C* **83** (2023) 31, arXiv:2205.06094 [gr-qc].

[33] L.-Y. Chen, H. Yu, and P. Wu, "Primordial non-Guassianity in inflation with gravitationally enhanced friction," *Phys. Rev. D* **106** (2022) 063537, arXiv:2210.05201 [gr-qc].

[34] D.-S. Meng, C. Yuan, and Q.-G. Huang, "Primordial black holes generated by the non-minimal spectator field," *Sci. China Phys. Mech. Astron.* **66** (2023) 280411, arXiv:2212.03577 [astro-ph.CO].

[35] Z.-Q. You, Z. Yi, and Y. Wu, "Constraints on primordial curvature power spectrum with pulsar timing arrays," *JCAP* **11** (2023) 065, arXiv:2307.04419 [gr-qc].

[36] **NANOGrav** Collaboration, G. Agazie *et al.*, "The NANOGrav 15 yr Data Set: Observations and Timing of 68 Millisecond Pulsars," *Astrophys. J. Lett.* **951** (2023) L9, arXiv:2306.16217 [astro-ph.HE].

[37] **NANOGrav** Collaboration, G. Agazie *et al.*, "The NANOGrav 15 yr Data Set: Evidence for a Gravitational-wave Background," *Astrophys. J. Lett.* **951** (2023) L8, arXiv:2306.16213

[astro-ph.HE].

[38] A. Zic *et al.*, "The Parkes Pulsar Timing Array third data release," *Publ. Astron. Soc. Austral.* **40** (2023) e049, arXiv:2306.16230 [astro-ph.HE].

[39] D. J. Reardon *et al.*, "Search for an Isotropic Gravitational-wave Background with the Parkes Pulsar Timing Array," *Astrophys. J. Lett.* **951** (2023) L6, arXiv:2306.16215 [astro-ph.HE].

[40] **EPTA** Collaboration, J. Antoniadis *et al.*, "The second data release from the European Pulsar Timing Array - I. The dataset and timing analysis," *Astron. Astrophys.* **678** (2023) A48, arXiv:2306.16224 [astro-ph.HE].

[41] **EPTA, InPTA:** Collaboration, J. Antoniadis *et al.*, "The second data release from the European Pulsar Timing Array - III. Search for gravitational wave signals," *Astron. Astrophys.* **678** (2023) A50, arXiv:2306.16214 [astro-ph.HE].

[42] H. Xu *et al.*, "Searching for the Nano-Hertz Stochastic Gravitational Wave Background with the Chinese Pulsar Timing Array Data Release I," *Res. Astron. Astrophys.* **23** (2023) 075024, arXiv:2306.16216 [astro-ph.HE].

[43] P. Ivanov, P. Naselsky, and I. Novikov, "Inflation and primordial black holes as dark matter," *Phys. Rev. D* **50** (1994) 7173–7178.

[44] P. Ivanov, "Nonlinear metric perturbations and production of primordial black holes," *Phys. Rev. D* **57** (1998) 7145–7154, arXiv:astro-ph/9708224.

[45] C. Germani and T. Prokopec, "On primordial black holes from an inflection point," *Phys. Dark Univ.* **18** (2017) 6–10, arXiv:1706.04226 [astro-ph.CO].

[46] J. Garcia-Bellido and E. Ruiz Morales, "Primordial black holes from single field models of inflation," *Phys. Dark Univ.* **18** (2017) 47–54, arXiv:1702.03901 [astro-ph.CO].

[47] H. Motohashi and W. Hu, "Primordial Black Holes and Slow-Roll Violation," *Phys. Rev. D* **96** (2017) 063503, arXiv:1706.06784 [astro-ph.CO].

[48] G. Ballesteros and M. Taoso, "Primordial black hole dark matter from single field inflation," *Phys. Rev. D* **97** (2018) 023501, arXiv:1709.05565 [hep-ph].

[49] N. Bhaumik and R. K. Jain, "Primordial black holes dark matter from inflection point models of inflation and the effects of reheating," *JCAP* **01** (2020) 037, arXiv:1907.04125 [astro-ph.CO].

[50] S. S. Mishra and V. Sahni, "Primordial Black Holes from a tiny bump/dip in the Inflaton potential," *JCAP* **04** (2020) 007, arXiv:1911.00057 [gr-qc].

[51] S. Kachru, R. Kallosh, A. D. Linde, and S. P. Trivedi, "De Sitter vacua in string theory," *Phys. Rev. D* **68** (2003) 046005, arXiv:hep-th/0301240.

[52] S. Kachru, R. Kallosh, A. D. Linde, J. M. Maldacena, L. P. McAllister, and S. P. Trivedi, "Towards inflation in string theory," *JCAP* **10** (2003) 013, arXiv:hep-th/0308055.

[53] D. Baumann, "Inflation," arXiv:0907.5424 [hep-th].

[54] M. Sasaki, "Large Scale Quantum Fluctuations in the Inflationary Universe," *Prog. Theor. Phys.* **76** (1986) 1036.

[55] V. F. Mukhanov, "Quantum Theory of Gauge Invariant Cosmological Perturbations," *Sov. Phys. JETP* **67** (1988) 1297–1302.

[56] T. S. Bunch and P. C. W. Davies, "Quantum Field Theory in de Sitter Space: Renormalization by Point Splitting," *Proc. Roy. Soc. Lond. A* **360** (1978) 117–134.

[57] K. A. Malik and D. Wands, "Cosmological perturbations," *Phys. Rept.* **475** (2009) 1–51, arXiv:0809.4944 [astro-ph].

[58] J. R. Espinosa, D. Racco, and A. Riotto, "A Cosmological Signature of the SM Higgs Instability: Gravitational Waves," *JCAP* **09** (2018) 012, arXiv:1804.07732 [hep-ph].

[59] S. Borsanyi *et al.*, "Calculation of the axion mass based on high-temperature lattice quantum

chromodynamics," *Nature* **539** (2016) 69–71, arXiv:1606.07494 [hep-lat].

[60] M. Sasaki, T. Suyama, T. Tanaka, and S. Yokoyama, "Primordial black holes—perspectives in gravitational wave astronomy," *Class. Quant. Grav.* **35** (2018) 063001, arXiv:1801.05235 [astro-ph.CO].

[61] K. Inomata, M. Kawasaki, K. Mukaida, Y. Tada, and T. T. Yanagida, "Inflationary Primordial Black Holes as All Dark Matter," *Phys. Rev. D* **96** (2017) 043504, arXiv:1701.02544 [astro-ph.CO].

[62] W. H. Press and P. Schechter, "Formation of galaxies and clusters of galaxies by selfsimilar gravitational condensation," *Astrophys. J.* **187** (1974) 425–438.

[63] T. Harada, C.-M. Yoo, and K. Kohri, "Threshold of primordial black hole formation," *Phys. Rev. D* **88** (2013) 084051, arXiv:1309.4201 [astro-ph.CO]. [Erratum: Phys.Rev.D 89, 029903 (2014)].

[64] V. Atal, J. Garriga, and A. Marcos-Caballero, "Primordial black hole formation with non-Gaussian curvature perturbations," *JCAP* **09** (2019) 073, arXiv:1905.13202 [astro-ph.CO].

[65] R. Kallosh, A. Linde, and Y. Yamada, "Planck 2018 and Brane Inflation Revisited," *JHEP* **01** (2019) 008, arXiv:1811.01023 [hep-th].

[66] R. Kallosh and A. Linde, "On hilltop and brane inflation after Planck," *JCAP* **09** (2019) 030, arXiv:1906.02156 [hep-th].

[67] R. Kallosh and A. Linde, "CMB targets after the latest Planck data release," *Phys. Rev. D* **100** (2019) 123523, arXiv:1909.04687 [hep-th].

[68] R. Kallosh and A. Linde, "B-mode Targets," *Phys. Lett. B* **798** (2019) 134970, arXiv:1906.04729 [astro-ph.CO].

[69] S. Bird, H. V. Peiris, M. Viel, and L. Verde, "Minimally Parametric Power Spectrum Reconstruction from the Lyman-alpha Forest," *Mon. Not. Roy. Astron. Soc.* **413** (2011) 1717–1728, arXiv:1010.1519 [astro-ph.CO].

[70] D. J. Fixsen, E. S. Cheng, J. M. Gales, J. C. Mather, R. A. Shafer, and E. L. Wright, "The Cosmic Microwave Background spectrum from the full COBE FIRAS data set," *Astrophys. J.* **473** (1996) 576, arXiv:astro-ph/9605054.

[71] B. Kavanagh, "bradkav/PBHbounds: Release version (1.0). Zenodo," 2019.

[72] **Planck** Collaboration, Y. Akrami *et al.*, "Planck 2018 results. X. Constraints on inflation," *Astron. Astrophys.* **641** (2020) A10, arXiv:1807.06211 [astro-ph.CO].

[73] **EPTA** Collaboration, L. Lentati *et al.*, "European Pulsar Timing Array Limits On An Isotropic Stochastic Gravitational-Wave Background," *Mon. Not. Roy. Astron. Soc.* **453** (2015) 2576–2598, arXiv:1504.03692 [astro-ph.CO].

[74] R. M. Shannon *et al.*, "Gravitational waves from binary supermassive black holes missing in pulsar observations," *Science* **349** (2015) 1522–1525, arXiv:1509.07320 [astro-ph.CO].

[75] **NANOGrav** Collaboration, G. Agazie *et al.*, "The NANOGrav 15 yr Data Set: Detector Characterization and Noise Budget," *Astrophys. J. Lett.* **951** (2023) L10, arXiv:2306.16218 [astro-ph.HE].

[76] K. Schmitz, "New Sensitivity Curves for Gravitational-Wave Signals from Cosmological Phase Transitions," *JHEP* **01** (2021) 097, arXiv:2002.04615 [hep-ph].

[77] **LISA** Collaboration, P. Amaro-Seoane *et al.*, "Laser Interferometer Space Antenna," arXiv:1702.00786 [astro-ph.IM].

[78] W.-H. Ruan, Z.-K. Guo, R.-G. Cai, and Y.-Z. Zhang, "Taiji program: Gravitational-wave sources," *Int. J. Mod. Phys. A* **35** (2020) 2050075, arXiv:1807.09495 [gr-qc].

[79] **TianQin** Collaboration, J. Luo *et al.*, "TianQin: a space-borne gravitational wave detector," *Class. Quant. Grav.* **33** (2016) 035010, arXiv:1512.02076 [astro-ph.IM].

[80] S. Kawamura *et al.*, "The Japanese space gravitational wave antenna: DECIGO," *Class. Quant.*

Grav. **28** (2011) 094011.

[81] J. Crowder and N. J. Cornish, "Beyond LISA: Exploring future gravitational wave missions," *Phys. Rev. D* **72** (2005) 083005, arXiv:gr-qc/0506015.

[82] **KAGRA, LIGO Scientific, Virgo** Collaboration, B. P. Abbott *et al.*, "Prospects for observing and localizing gravitational-wave transients with Advanced LIGO, Advanced Virgo and KAGRA," *Living Rev. Rel.* **19** (2016) 1, arXiv:1304.0670 [gr-qc].

[83] **LIGO Scientific** Collaboration, B. P. Abbott *et al.*, "Exploring the Sensitivity of Next Generation Gravitational Wave Detectors," *Class. Quant. Grav.* **34** (2017) 044001, arXiv:1607.08697 [astro-ph.IM].

[84] **NANOGrav** Collaboration, A. Afzal *et al.*, "The NANOGrav 15 yr Data Set: Search for Signals from New Physics," *Astrophys. J. Lett.* **951** (2023) L11, arXiv:2306.16219 [astro-ph.HE]. [Erratum: Astrophys.J.Lett. 971, L27 (2024), Erratum: Astrophys.J. 971, L27 (2024)].

[85] **EPTA, InPTA** Collaboration, J. Antoniadis *et al.*, "The second data release from the European Pulsar Timing Array - IV. Implications for massive black holes, dark matter, and the early Universe," *Astron. Astrophys.* **685** (2024) A94, arXiv:2306.16227 [astro-ph.CO].

[86] C. Germani and I. Musco, "Abundance of Primordial Black Holes Depends on the Shape of the Inflationary Power Spectrum," *Phys. Rev. Lett.* **122** (2019) 141302, arXiv:1805.04087 [astro-ph.CO].

[87] M. Shibata and M. Sasaki, "Black hole formation in the Friedmann universe: Formulation and computation in numerical relativity," *Phys. Rev. D* **60** (1999) 084002, arXiv:gr-qc/9905064.

[88] I. Musco, J. C. Miller, and A. G. Polnarev, "Primordial black hole formation in the radiative era: Investigation of the critical nature of the collapse," *Class. Quant. Grav.* **26** (2009) 235001, arXiv:0811.1452 [gr-qc].

[89] A. G. Polnarev and I. Musco, "Curvature profiles as initial conditions for primordial black hole formation," *Class. Quant. Grav.* **24** (2007) 1405–1432, arXiv:gr-qc/0605122.

[90] A. Escrivà, C. Germani, and R. K. Sheth, "Universal threshold for primordial black hole formation," *Phys. Rev. D* **101** (2020) 044022, arXiv:1907.13311 [gr-qc].

[91] A. Escrivà, "Simulation of primordial black hole formation using pseudo-spectral methods," *Phys. Dark Univ.* **27** (2020) 100466, arXiv:1907.13065 [gr-qc].

[92] P. De la Torre Luque, J. Koechler, and S. Balaji, "Refining Galactic primordial black hole evaporation constraints," *Phys. Rev. D* **110** (2024) 123022, arXiv:2406.11949 [astro-ph.HE].

[93] H. Niikura, M. Takada, S. Yokoyama, T. Sumi, and S. Masaki, "Constraints on Earth-mass primordial black holes from OGLE 5-year microlensing events," *Phys. Rev. D* **99** (2019) 083503, arXiv:1901.07120 [astro-ph.CO].

[94] P. Mróz *et al.*, "Limits on Planetary-mass Primordial Black Holes from the OGLE High-cadence Survey of the Magellanic Clouds," *Astrophys. J. Lett.* **976** (2024) L19, arXiv:2410.06251 [astro-ph.CO].

[95] M. Zumalacarregui and U. Seljak, "Limits on stellar-mass compact objects as dark matter from gravitational lensing of type Ia supernovae," *Phys. Rev. Lett.* **121** (2018) 141101, arXiv:1712.02240 [astro-ph.CO].

[96] **Macho** Collaboration, R. A. Allsman *et al.*, "MACHO project limits on black hole dark matter in the 1-30 solar mass range," *Astrophys. J. Lett.* **550** (2001) L169, arXiv:astro-ph/0011506.

[97] D. Croon, D. McKeen, N. Raj, and Z. Wang, "Subaru-HSC through a different lens: Microlensing by extended dark matter structures," *Phys. Rev. D* **102** (2020) 083021, arXiv:2007.12697 [astro-ph.CO].

[98] **EROS-2** Collaboration, P. Tisserand *et al.*, "Limits on the Macho Content of the Galactic Halo

from the EROS-2 Survey of the Magellanic Clouds," *Astron. Astrophys.* **469** (2007) 387–404, arXiv:astro-ph/0607207.

[99] M. Oguri, J. M. Diego, N. Kaiser, P. L. Kelly, and T. Broadhurst, "Understanding caustic crossings in giant arcs: characteristic scales, event rates, and constraints on compact dark matter," *Phys. Rev. D* **97** (2018) 023518, arXiv:1710.00148 [astro-ph.CO].

[100] T. Blaineau *et al.*, "New limits from microlensing on Galactic black holes in the mass range 10 M$\odot$ < M < 1000 M$\odot$," *Astron. Astrophys.* **664** (2022) A106, arXiv:2202.13819 [astro-ph.GA].

[101] A. Esteban-Gutiérrez, E. Mediavilla, J. Jiménez-Vicente, and J. A. Muñoz, "Constraints on the Abundance of Primordial Black Holes from X-Ray Quasar Microlensing Observations: Substellar to Planetary Mass Range," *Astrophys. J.* **954** (2023) 172, arXiv:2307.07473 [astro-ph.CO].

[102] C. Leung *et al.*, "Constraining primordial black holes using fast radio burst gravitational-lens interferometry with CHIME/FRB," *Phys. Rev. D* **106** (2022) 043017, arXiv:2204.06001 [astro-ph.HE].

[103] **LIGO Scientific, Virgo** Collaboration, B. P. Abbott *et al.*, "Search for Subsolar Mass Ultracompact Binaries in Advanced LIGO's Second Observing Run," *Phys. Rev. Lett.* **123** (2019) 161102, arXiv:1904.08976 [astro-ph.CO].

[104] B. J. Kavanagh, D. Gaggero, and G. Bertone, "Merger rate of a subdominant population of primordial black holes," *Phys. Rev. D* **98** (2018) 023536, arXiv:1805.09034 [astro-ph.CO].

[105] T. Boybeyi, S. Clesse, S. Kuroyanagi, and M. Sakellariadou, "Search for a gravitational wave background from primordial black hole binaries using data from the first three LIGO-Virgo-KAGRA observing runs," *Phys. Rev. D* **112** (2025) 023551, arXiv:2412.18318 [astro-ph.CO].

[106] Z.-C. Chen and Q.-G. Huang, "Distinguishing Primordial Black Holes from Astrophysical Black Holes by Einstein Telescope and Cosmic Explorer," *JCAP* **08** (2020) 039, arXiv:1904.02396 [astro-ph.CO].

[107] A. H. Nitz and Y.-F. Wang, "Broad search for gravitational waves from subsolar-mass binaries through LIGO and Virgo's third observing run," *Phys. Rev. D* **106** (2022) 023024, arXiv:2202.11024 [astro-ph.HE].

[108] J. Manshanden, D. Gaggero, G. Bertone, R. M. T. Connors, and M. Ricotti, "Multi-wavelength astronomical searches for primordial black holes," *JCAP* **06** (2019) 026, arXiv:1812.07967 [astro-ph.HE].

[109] P. D. Serpico, V. Poulin, D. Inman, and K. Kohri, "Cosmic microwave background bounds on primordial black holes including dark matter halo accretion," *Phys. Rev. Res.* **2** (2020) 023204, arXiv:2002.10771 [astro-ph.CO].

[110] A. Hektor, G. Hütsi, L. Marzola, M. Raidal, V. Vaskonen, and H. Veermäe, "Constraining Primordial Black Holes with the EDGES 21-cm Absorption Signal," *Phys. Rev. D* **98** (2018) 023503, arXiv:1803.09697 [astro-ph.CO].

[111] P. Lu, V. Takhistov, G. B. Gelmini, K. Hayashi, Y. Inoue, and A. Kusenko, "Constraining Primordial Black Holes with Dwarf Galaxy Heating," *Astrophys. J. Lett.* **908** (2021) L23, arXiv:2007.02213 [astro-ph.CO].

[112] M. A. Monroy-Rodríguez and C. Allen, "The end of the MACHO era- revisited: new limits on MACHO masses from halo wide binaries," *Astrophys. J.* **790** (2014) 159, arXiv:1406.5169 [astro-ph.GA].

[113] T. D. Brandt, "Constraints on MACHO Dark Matter from Compact Stellar Systems in Ultra-Faint Dwarf Galaxies," *Astrophys. J. Lett.* **824** (2016) L31, arXiv:1605.03665 [astro-ph.GA].

[114] V. Kalogera *et al.*, "The Next Generation Global Gravitational Wave Observatory: The Science Book," arXiv:2111.06990 [gr-qc].

[115] S. Jung and T. Kim, "Gamma-ray burst lensing parallax: Closing the primordial black hole dark matter mass window," *Phys. Rev. Res.* **2** (2020) 013113, arXiv:1908.00078 [astro-ph.CO].

[116] B. J. Carr, K. Kohri, Y. Sendouda, and J. Yokoyama, "New cosmological constraints on primordial black holes," *Phys. Rev. D* **81** (2010) 104019, arXiv:0912.5297 [astro-ph.CO].

[117] S. Clark, B. Dutta, Y. Gao, L. E. Strigari, and S. Watson, "Planck Constraint on Relic Primordial Black Holes," *Phys. Rev. D* **95** (2017) 083006, arXiv:1612.07738 [astro-ph.CO].

[118] R. Laha, J. B. Muñoz, and T. R. Slatyer, "INTEGRAL constraints on primordial black holes and particle dark matter," *Phys. Rev. D* **101** (2020) 123514, arXiv:2004.00627 [astro-ph.CO].

[119] X.-h. Tan and J.-q. Xia, "Revisiting bounds on primordial black hole as dark matter with X-ray background," *JCAP* **09** (2024) 022, arXiv:2404.17119 [astro-ph.CO].

[120] M. Boudaud and M. Cirelli, "Voyager 1 $e^{\pm}$ Further Constrain Primordial Black Holes as Dark Matter," *Phys. Rev. Lett.* **122** (2019) 041104, arXiv:1807.03075 [astro-ph.HE].

[121] S. Mittal, A. Ray, G. Kulkarni, and B. Dasgupta, "Constraining primordial black holes as dark matter using the global 21-cm signal with X-ray heating and excess radio background," *JCAP* **03** (2022) 030, arXiv:2107.02190 [astro-ph.CO].

[122] K. Griest, A. M. Cieplak, and M. J. Lehner, "Experimental Limits on Primordial Black Hole Dark Matter from the First 2 yr of Kepler Data," *Astrophys. J.* **786** (2014) 158, arXiv:1307.5798 [astro-ph.CO].

[123] B. Carr, K. Kohri, Y. Sendouda, and J. Yokoyama, "Constraints on primordial black holes," *Rept. Prog. Phys.* **84** (2021) 116902, arXiv:2002.12778 [astro-ph.CO].

[124] S. K. Acharya and R. Khatri, "CMB and BBN constraints on evaporating primordial black holes revisited," *JCAP* **06** (2020) 018, arXiv:2002.00898 [astro-ph.CO].

[125] S. W. Hawking, "Black hole explosions," *Nature* **248** (1974) 30–31.